Transport and Absorption of Anesthetic Vapors in a Mouth-Lung Model Extending to G9 Bronchioles

Jinxiang Xi[1,*], JongWon Kim[1] and Xiuhua A. Si[2]

[1]*Department of Mechanical and Biomedical Engineering, Central Michigan University, Mount Pleasant, MI, USA*

[2]*Department of Engineering, Calvin College, Grand Rapids, MI, USA*

Abstract: *Background*: The inhalation of anesthetic vapors into the lungs is a function of both the respiration and inhalant property. Factors which influence the alveolar concentration of anesthetics include breathing activities, airway morphology, anesthetic diffusivity, and wall absorption rate. Administered anesthetic levels could be significantly different from the alveolar level due to wall absorption loss and gas mixing in the airway.

Objective: To assess the transport and absorption of inhaled anesthetics in an anatomically accurate respiratory airway geometry. Specifically aims include understanding the transport of inhaled vapors, quantifying the pulmonary dosage of administered anesthetics, and identifying factors that influence airway absorption losses.

Methods: The geometry consisted of a CT-based mouth-throat (MT) model and a tracheobronchial (TB) model which extends to G9 bronchioles and consists of 115 outlets. Vapor transport and absorption were simulated using the Chemical Species model coupled with a user-defined vapor-absorption module.

Results: Unlike previously assumed developed flows after G6, features of developing flows are still apparent in the G9 bronchioles in this study. Large variations of bronchiolar vapor concentrations were observed among the five lobes. Under quiet breathing conditions, vapor concentrations at the G9 outlets are 15 – 30% of the inhaled concentration level due to gas mixing and wall absorption. The delivered dose to the pulmonary region varies from 48% to 96%, depending on the vapor diffusivity and solubility. Vapor depletion due to wall absorption is significant (52%) for highly soluble anesthetics and is inconsequential for low solubility ones.

Conclusion: A computer model was developed that implemented a wall absorption module in a realistic mouth-lung model extending to G9. This model provides the basis for future quantitative studies of the relationship between administered anesthetics and induced anesthetic level.

Keywords: Vapor transport, wall absorption, inhalation anesthetics, ultrafine aerosols, lung model.

1. INTRODUCTION

Inhalation anesthetics are frequently administered for the purpose to relieve the pain of surgery. Commonly administered anesthetics include volatile liquids such as isoflurane, halothane, sevoflurane and desflurane, and inorganic gas, such as xenon and nitrous oxide [1]. Inhalant anesthetics are generally administered to the patients either by face masks, endotracheal tubes, or enclosed chambers containing anesthetic vapors. Once the anesthetic agents are ventilated into the alveolar, they will be absorbed into the blood and distributed to different tissues, with the brain being the main target. Inhaled anesthetics act in different ways at the level of the central nervous system to induce a local or general loss of sensation. They suppress nerve responses to sensory stimulation either by amplifying the inhibitory function or decreasing excitatory transmission at the nerve endings in the brain [2]. The induced anesthesia is usually categorized into four levels, as listed in Table **1**, which can be monitored by heart rate, respiration rhythm, pupil reflexes, and spontaneous eye movements. For example, the stage IV anesthesia is indicated by the loss of spontaneous respiration and the imminent collapse of cardiovascular control, which should be avoided during the surgery. One key issue of inhalation anesthesia is how to closely control the level of anesthesia during the surgical process. However, the relationship between the administered amount of anesthetic and the anesthetic level is complex, which involves the dosage to the lung, the transfusion and transportation in the blood, and the uptake by the sensory nerves. The mechanism by which inhaled anesthetics produce the CNS depression is not clearly understood, and a single theory to explain it is unlikely [3,4].

The standard index of the level of inhalation anesthetics is the minimum alveolar concentration (MAC), which defines the minimal level of anesthesia necessary to permit surgery [5]. Factors governing the alveolar concentration of inhalants include inspired concentration, alveolar ventilation, solubility, cardiac output, and blood flow to the tissues. Inhalational

*Address correspondence to this author at the Department of Mechanical and Biomedical Engineering, Central Michigan University, 1200 South Franklin Street, Mount Pleasant, MI 48858, USA; Tel: (989) 774-2456;
Fax: (989) 774-4900; E-mail: xi1j@cmich.edu

E-ISSN: 2310-9394/13

Table 1: Four Stages of Inhalation Anesthesia

	Also known as	Period	Symptoms
Stage 1	Induction	Between initial administration and loss of consciousness.	Patient progresses from analgesia without amnesia to analgesia. Patients can carry on a conversation.
Stage 2	Excitement stage	After loss of consciousness and marked by excited and delirious activity.	Uncontrolled movements, vomiting, breathe holding, pupillary dilation.
Stage 3	Surgical anesthesia	Phase 1	Eyes initially rolling, then becoming fixed
		Phase 2	Loss of corneal and laryngeal reflexes.
		Phase 3	Pupils dilate and loss of light reflex.
		Phase 4	Paralysis, shallow abdominal respiration
Stage 4	Overdose	Patient has severe brain stem or medullary depression.	Cessation of respiration and potential cardiovascular collapse.

anesthetics can be delivered through a facemask or a tracheal tube connected to an anesthetic vaporizer. The better a patient breathes in, the better the gas exchanges, and the faster the patient gets anesthetized. Clinically, the alveolar anesthetic gas levels are difficult to measure; the end tidal levels of inhalant anesthetics are generally used as an approximation to the alveolar gas tensions [6]. However, the alveoli anesthetic levels are different from the inhaled levels after the anesthetic vapors traveling through the complex reparatory tract where wall absorption and gas exchange occur. Vapor or nanoparticles have been shown to be absorbed/deposited at high concentrations in the extrathoracic airway [7]. This absorption/deposition loss can be further compounded by particle characteristics, airflow field, and the airway geometry [8-11]. Therefore, understanding the uptake and elimination of an inhalational anesthetic is necessary for their proper use and for improved patient safety.

Due to small sizes and low Stokes numbers (inertia force), vapor and ultrafine particles are typically considered analogous in their behaviors in the respiratory tract as both are predominately governed by the Brownian motion. A number of *in vivo* studies have considered absorption/depositions of vapor and ultrafine aerosols in human subjects [7,12-16]. Cheng *et al*. [7] measured the nasal and oral deposition of ultrafine aerosols in 10 normal adult male subjects, and reported significant variations among the subjects. *In vitro* studies that have considered flow field and ultrafine particle deposition in human extrathoracic airway geometries include Heenan *et al*. [17], Johnstone *et al*. [18] , Zhang *et al*. [19,20], Cheng *et al*. [21,22]. Heenan *et al*. [17] compared the flow field in a mouth-throat model between measurements and simulation and showed that Reynolds Averaged Nervier-Stokes (RANS) turbulence models didn't adequately capture the increased viscous effects at lower Reynolds numbers. They attributed the deficiency of RANS models to inadequate boundary modeling, transitional flow regimes, and curvature-related anisotropic turbulence. Zhang *et al*. [20] compared measurements with existing *in vivo* data and indicated that current USP throats couldn't sufficiently represent realistic extrathoracic airway geometries. A design optimization of the proposed idealized mouth-throat was later performed by Zhang *et al*. [19]. The results showed that different key dimensions are required for different flow rates in order to adequately reproduce the *in vivo* extrathoracic depositions. In addition to *in vivo* and *in vitro* experiments, a number of numerical studies have considered the transport and wall absorption of inhaled vapors [23-26] and ultrafine particles [27,28]. The mass transport of chemical species within the airway walls is controlled by inhalant solubility, diffusion, and wall structure. Some studies assumed high reactivity of the inhaled vapor and a zero concentration condition [25,29,26]. Studies that considered solubility in a mucus layer include Zhao *et al*. [30], Keyhani *et al*. [31], and Tian and Longest [32,33]. In light of ultrafine particles, Hofmann *et al*. [27] employed a Lagrangian particle tracking model for dilute ultrafine aerosols in a model of the third-to-fourth airway junction. Xi el al. [28] studied the laryngeal effect on airflow and nanoparticle depositions in a cast-based TB model extending to G6 and observed that turbulent effect persisted into the fourth generation (G4) of the lungs. In addition, the larynx exerted a substantial impact on the accumulation of inhaled nanoparticles.

In summary, many studies have investigated the vapor or nanoparticle absorption/depositions either in human subjects, replica casts, or computer models,

and have also shown significant impacts of geometric realism on flow fields, vapor absorptions, and particle depositions. However, few studies have studied vapor or nanoparticle absorption/deposition in the airway that extends beyond G6. One of the exceptions is Tian *et al.* [34] who simulated nanoparticle condensation growth in a single path model that extended to G15. However, this model had only one branch bifurcation in each generation after G3, and evaluation of its adequacy in representing a tree of lung branches is still in adolescence.

The objective of this study is to assess the transport and absorption of inhaled anesthetics in a physiologically realistic MT-TB geometry that extends to G9. Specific aims include: (1) quantifying the pulmonary dosage of administered anesthetics, (2) identifying factors that influence upper airway wall absorption, and (3) characterizing where the absorption loss occurs. Benefits from this study include better understanding of vapor absorption in deep lungs, and new guidelines to improve the delivery of inhalation anesthetics.

2. METHODS

2.1. Construction of Mouth-Lung Model

The geometry considered in this study consists of the mouth-throat (MT) region, the upper tracheobronchial (TB) airways extending from the trachea to the generation nine (G9) bronchioles (Figure **1**). The trachea and two main bronchi constitute the bifurcation G1. The MT geometry is a modification of the physiologically realistic model proposed by Xi and Longest [35] and contains the oral cavity, pharynx, and larynx. This geometry was based on the oral airway cast reported by Cheng *et al*. [36] along with in-house CT data of the pharynx and larynx. The main geometric features retained in the realistic model include the airway curvature from the mouth entrance to the throat, an oral cavity with a half mouth opening, a triangular-shaped glottis, and a dorsal-angled upper trachea. More anatomical details such as the epiglottal fold and laryngeal sinus have been added to the pharynx and larynx. Both of these anatomies are expected to influence aerosol dynamics and are intended to improve the realism of the model.

The TB geometry was based on the anatomical cast dimensions reported by Yeh and Schum [37] and scaled to a functional residual capacity (FRC) of 3.5 L, which is consistent with an adult male [38]. The three major features of this physiologically realistic TB model are the right-left asymmetry, the cartilage rings, and the non-planar of bifurcating branches. There are two lobes (upper and lower) in the left lung and three lobes (upper, middle, and lower) in the right lung. Similarly, ventilation to the right and let lungs is also asymmetric.

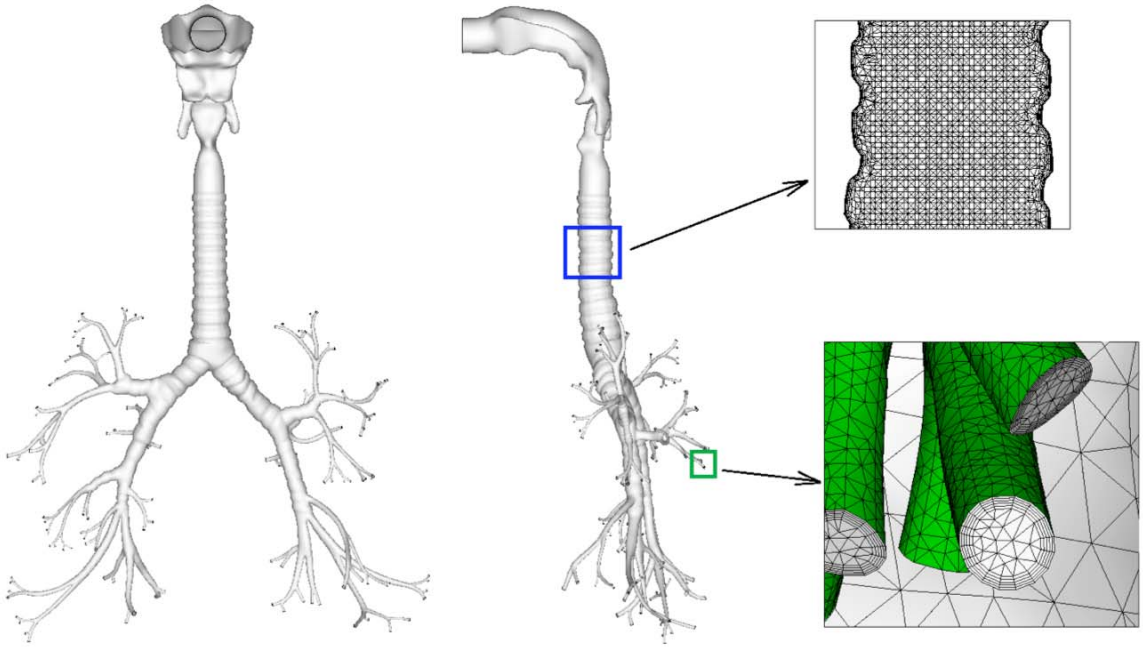

(**a**) (**b**)

Figure 1: Image-based mouth-lung model: (**a**) surface model and (**b**) computational mesh. The mesh consists of approximately six million unstructured tetrahedral elements and a fine near-wall pentahedral grid.

According to measurements by Cohen *et al*. [39], the left lungs receives approximately 40% of the inhaled air, with 16% feeding into the left upper (LU) lobe and 24% into the left lower (LL) lobe. The 60% ventilation to the right lung distributes approximately 18% to the right upper (RU) lobe, 12% to the right middle (RM) lobe, and 30% to the right lower (RL) lobe.

C-shaped cartilage rings were kept in the TB model through the trachea to the bifurcation G4, which prevent these airways from collapsing during absence of air [40]. Surface properties of the bifurcations such as the carina ridge were taken from the measurements of Horsfield *et al*. [41] and Hammersley and Olson [42]. The bifurcation units were rotated out of plane to approximate the gravity angles specified by Yeh and Schum [37]. The branch diameters, lengths, and bifurcation angles of each generation were consistent with those reported by Heistracher and Hofmann [43], with only slight modifications that were required to generate smooth asymmetrical bifurcations. In the resulting airway model, the trachea had an average diameter of 19 mm and a length of 90 mm. The diameters of the right and left main bronchi were 14.3 and 14.1 mm, and the lengths of the two bronchi were 23 and 57.5 mm, respectively. Some distal branches in the range of generations G8 and G9 were not retained in the TB model. Most of the model paths extended from the trachea to generation G7 with some paths extending to generations G8 and G9. As a result, a total of 115 outlets were preserved in the final computational model. The resultant mouth-TB model in this study is intended to be a general representation of adult human airways that includes pharyngeal details, lung asymmetry, bifurcation out-of-plane rotation, and previously documented branching parameters.

2.2. Continuous and Discrete Phase Transport Equations

2.2.1. LRN k-ω Turbulence Model

Flows in all the geometries considered are assumed to be isothermal and incompressible. Both the laminar and the low Reynolds number (LRN) k-ω turbulence model have been employed in order to simulate the laminar, transitional and fully turbulent flow regimes of interest. The LRN k-ω model was selected based on its ability to accurately predict pressure drop, velocity profiles and shear stress for transitional and turbulent flows [44,45]. This model has also been demonstrated to accurately predict aerosol deposition profiles for transitional and turbulent flows in models of the oral airway [46,47] and multiple bifurcations [48]. Moreover, the LRN k-ω model has been shown to provide an accurate solution for laminar flow as the turbulent viscosity approaches zero [45].

2.2.2. Continuous Chemical Species Model

In this study, a standard chemical species (CS) model and a well-tested discrete Lagrangian tracking model were implemented to simulate the dynamics of pharmaceutical colloids. For the CS model, the mass transport relation governing the convective-diffusive motion of ultrafine aerosols can be written as

$$\frac{\partial c}{\partial t}+\frac{\partial\left(u_j c\right)}{\partial x_j}=\frac{\partial}{\partial x_j}\left[\left(\tilde{D}+\frac{\nu_T}{Sc_T}\right)\frac{\partial c}{\partial x_j}\right] \quad (1)$$

where *c* is the mass fraction of nanoparticles, $\tilde{D}$ is the molecular or Brownian diffusion coefficient and Sc_T is the turbulent Schmidt number, taken to be 0.9. Assuming dilute concentrations of spherical particles, the Stokes-Einstein equation is used to determine the diffusion coefficients

$$\tilde{D}=\frac{k_B T C_c}{3\pi\mu d_p} \quad (2)$$

where k_B = 1.38×10^{-16} cm^2g/s is the Boltzmann constant. The Cunningham correction factor is computed using the expression of Allen and Raabe [49]

$$C_c=1+\frac{\lambda}{d_p}\left(2.34+1.05\exp\left(-0.39\frac{d_p}{\lambda}\right)\right) \quad (3)$$

where λ is the mean free path of air, assumed to be 65 nm.

2.2.3. Absorption Model at the Air-Wall Interface

An analytical boundary condition that considered the mass transport at the air-wall interface was implemented in this study. The airway wall consists of mucus, tissue, and capillary vessels and can be considered as a composite layer. Based on ICRP [38], the height of the airway wall h_w in different airway regions are listed in Table **2** [32]. Convection is negligible in the wall and zero concentration of the absorbed chemical species is assumed at the outer layer. The governing equation of vapor concentration at the air-wall interface are adapted from Tian and Longest [32,33] and can be expressed as,

$$\frac{dC}{dn}+\frac{\tilde{D}_w\lambda_{a-w}}{\tilde{D}h_w}\cdot C=0 \quad (2)$$

where *n* is the height in the normal direction, $\tilde{D}_w$ is the vapor diffusivity in the compost wall layer, and λ_{a-w} is the air-wall partition coefficient. Species with λ_{a-w} >> 1 are considered to be highly soluble in the mucus and tissue, and coefficients in the range of 1 represent moderately soluble species [32,33]. Nearly all volatile anesthetic agents are hydrophobic and dissolve better in oil than in water. In contrast, xenon is highly soluble in water.

Table 2: Thickness of Mucus and Tissue Layers in the Conducting Airway

Region	Mucus (μm)	Tissue (μm)
Mouth-Throat	15	50
Bronchial region G1-G3	11	55
Bronchiolar region G4-G9	6	15

2.3. Breathing Conditions

Steady state breathing, or square waveforms, were adopted in this study. Inhalation flow rates were based on the mean flow rates reported by Cheng *et al*. [50]. Sedentary, light, and heavy activity conditions have been considered. Breathing frequencies and tidal volumes have been converted to mean steady inhalation flow rates taking into account that inhalation only occurs for approximately one-half the breathing cycle. Specifically, the mean inhalation flow rate is defined as $Q_{in} = 2 f V_T$ where *f* is the breathing frequency converted to breaths per second and V_T is the tidal volume in cm^3 per breath. The resulting inspiration flow rates for the three activity conditions considered are 15, 30 and 60 L/min, respectively. For these flow rates and steady flow conditions, mean inlet Reynolds numbers are 973, 1,945, and 3,890, respectively. The associated maximum Reynolds number values for sedentary, light, and heavy activity conditions occurring in the larynx and assuming a mean hydraulic diameter of 10.52 mm are 1,997, 3,994 and 7,987, respectively.

Studies of respiratory flows typically assumed a constant, parabolic or blunt inlet profile [51,48,52-54]. Our previous studies in bifurcating geometries show good agreement with regional and localized *in vitro* experimental data based on an initially blunt profile [48]. Considering that the inhalation of ambient air will likely result in a blunt velocity profile, this inlet condition has been employed for all geometries considered and is defined as

$$u(r) = 1.2244 u_m \left(\frac{R - r}{R} \right)^{1/7} \quad (8)$$

where *r* is the inlet radial coordinate, u_m is the mean velocity and *R* is the outer radius of the inlet. This profile is similar to a constant velocity inlet, but provides a smooth transition to the no-slip wall condition. Constant concentrations of the inhaled mass fraction (c_{in}) have been assumed at all inlets. The diffusivity of common anesthetics are generally within the range of 5e-6 − 15e-6 m^2/s [55]. For example, the diffusivity of nitrous oxide in air is 14.3e-6 m^2/s [56].

2.4. Numerical Methods

Due to the high complexity and multi-scale dimensions of the model in this study, multi-domain meshing approach was applied with unstructured tetrahedral elements using ANSYS ICEMCFD. Convergence sensitivity analysis was conducted to ensure grid-independent predictions. The final mesh consisted of approximately six million tetrahedral elements and a fine near-wall pentahedral grid (Figure **1**). To solve the governing mass and momentum conservation equations in each of the cases considered, the CFD package Fluent 6 was employed. User-supplied Fortran and C programs were implemented for the calculation of initial particle profiles, wall mass flow rates, Brownian force [57], anisotropic turbulence effect [58,59], and near-wall velocity interpolation [57]. All transport equations were discretized at least of second order accuracy in space. A segregated implicit solver was employed to evaluate the resulting linear system of equations. This solver uses the Gauss-Seidel method in conjunction with an algebraic multi-grid approach to solve the linearized equations. The SIMPLEC algorithm was employed to evaluate pressure-velocity coupling. Convergence of the flow field solution was assumed when the normalized global mass residuals fell below 10-5 and the residual-iteration curves for all flow parameters become asymptotic.

3. RESULTS AND DISCUSSION

3.1. Deposition Model Validation

To validate the computational model used in this study, numerically predictions are compared with existing experimental results for the deposition of ultrafine and fine aerosols in the MT and TB regions. The numerical MT geometry used in this comparison is based on the *in vitro* model and was implemented in the upper airway geometry shown in Figure **1**. For flow rates of 4 and 10 L/min, predictions of the CFD model are observed to match the *in vitro* conditions to a high

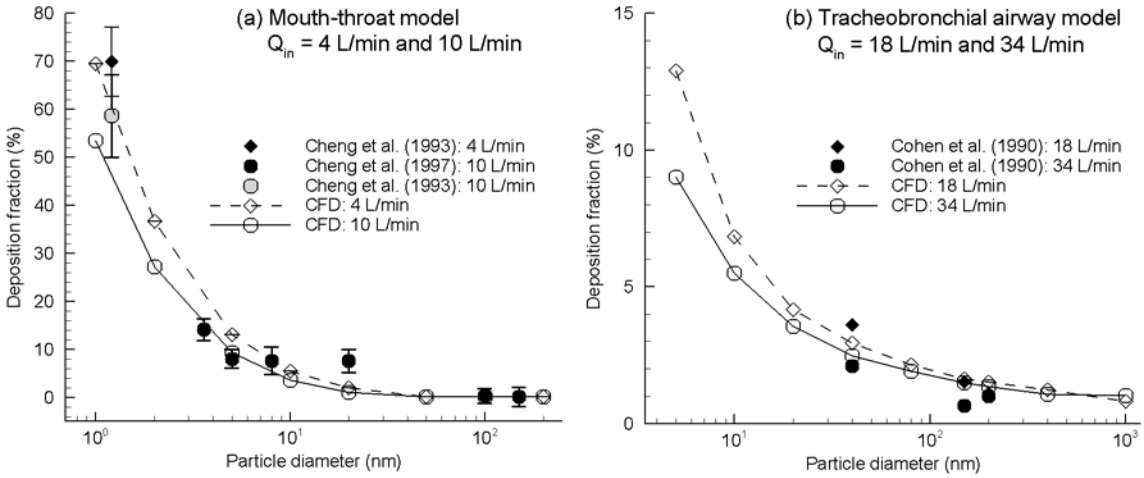

Figure 2: Comparison of nanoparticle deposition with existing experimental results for the (**a**) mouth-throat (MT) geometry, and (**b**) tracheobronchial (TB) region. Experimental data are presented as mean ± SD.

degree across a range of nanoparticle sizes. The deposition of nanoparticles in the TB geometry is compared to the *in vitro* results of Cohen *et al*. [39] in Figure **2b**. For this comparison, the numerical TB geometry including the larynx is a reproduction of the experimental model. Dilute submicrometer aerosols consistent with CSPs are considered at inhalation flow rates of 18 and 34 L/min. It is observed that the Lagrangian tracking model agrees with the *in vitro* results for both of the flow rate conditions considered. The use of user-defined BM and near-wall interpolation routines, as described by Longest and Xi [57], and near-wall anisotropic corrections were necessary to achieve agreement with the experimental data.

3.2. Velocity and Turbulence Fields

Detailed knowledge of aerodynamics is crucial in predicting the behavior and fates of inhaled agents. The velocity field and stream traces in the MT-TB geometry is illustrated in Figure **3** as sagittal and coronal contour profiles for an inhalation flow rate of 20 L/min. In Figure **3a**, skewed mid-plane velocity profiles are observed in the curved portion from the oral cavity to the larynx with the maximum velocity shifted to the dorsal wall of the pharynx region. This shift in the velocity profile is attributed to interactions among convective acceleration (i.e., inertial forces), boundary layer effects, and centrifugal forces in the curved bend. In the larynx, the airflow accelerates before the glottal aperture due to the gradual airway narrowing in this region. A laryngeal jet starts to form slightly upstream of the constricted glottis and propagates along the upper trachea. This jetting effect induces flow reversals near the left tracheal wall. As a result, a large recirculation zone develops, which in turn reduces the cross-sectional area available for expansion of the high-speed flow. This general phenomenon of jet instability is commonly referred to as the Coanda effect and has been reported in previous experimental investigations of the larynx during inhalation and exhalation [60-62]. In the cartilaginous rings, smaller eddies are noted (Figure **3c**). To illustrate the secondary motions in these regions, 2-D velocity contours and stream traces are shown in selected coronal slices (1-1' − 3-3' in Figure **3a**). The magnitude of the secondary motion in each slice is approximately 30% of the main flow. This secondary motion component functions to mix the inhaled air and distribute the inhaled air towards the wall.

Highly heterogeneous flow features are observed in the TB region (Figure **3a**, right panel), which arise from morphological details such as successive branching, left-right asymmetry, and non-planar bifurcations. The asymmetry is obvious in the two main bronchi. In the model considered, airflows in nearly all branches are still developing, and haven't reached a parabolic profile which characterizes developed laminar flows. Previous studies typically assumed developed flows in distal bronchioles after G6 [63,64]. However, results from this study clearly show the developing flow features as well as irregular velocity profiles even in G9 (Figure **3b**). Moreover, the velocity profiles in the distal bronchioles appear to differ significantly from one another. Therefore, a single-branch lung model as proposed in Tian *et al*. [34] may not adequately represent the whole lung scenario.

Turbulent characteristics within the nasal airway are displayed in Figure **4**. The turbulence viscosity ratio

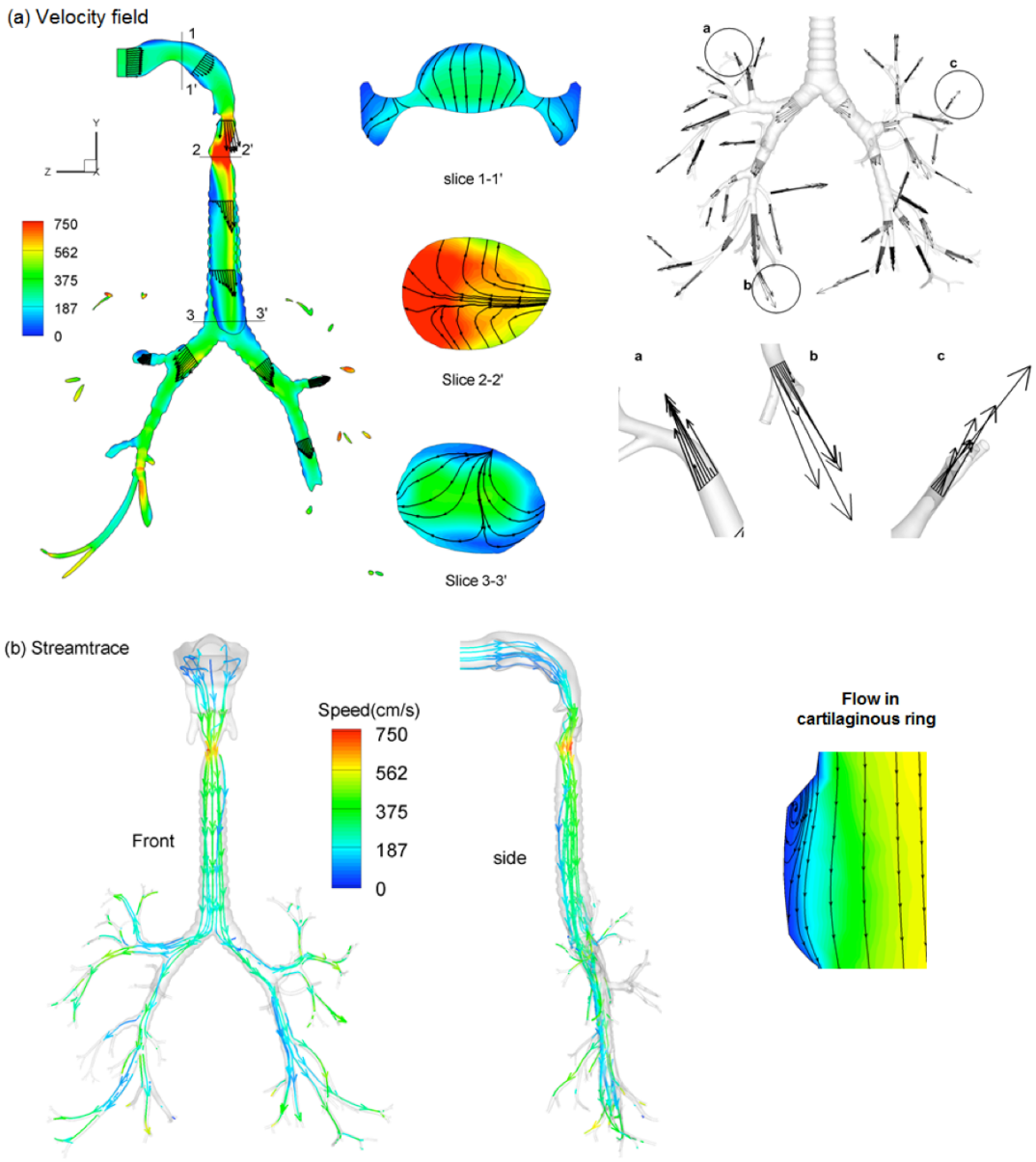

Figure 3: Inhalation airflow inside the respiratory tract at 20 L/min: (**a**) velocity field; (**b**) streamlines.

$\zeta = (\nu + \nu_t)/\nu$, where ν and ν_t are the laminar and turbulent kinematic viscosities, is a parameter that significantly affects aerosol dispersion and wall absorption. This parameter is proportional to turbulence intensity and represents the additional viscous transport due to turbulent mixing. From Figure **4**, turbulence occurs mainly in the larynx and the TB region. The turbulence peak inside the trachea may be attributed to both laryngeal jet effects and cartilaginous perturbations. The oral cavity and distal bronchioles are still dominated by laminar flows.

3.3. Vapor Transport

Steady state mass fraction contours of inhaled xenon vapor in the MT-TB geometry are displayed in Figure **6** for an inhalation flow rate of 20 L/min. Upon inhalation, anesthetic vapor starts to interact and mix with the airflow and is transported to the deep lungs. The concentration profile is attenuated along the axial stream direction as a result of enhanced mixing and wall absorption. This concentration decrease is further illustrated in the cross-sectional slices of Figure **5**. A direct comparison of airflow and particle transport patterns (Figure **3** vs. **5**) is informative. Dense vapor concentrations are observed to associate with areas of high flow velocities due to rapid convective mass transfer. Similarly, low particle concentrations occur either within recirculation zones or low-velocity regions. More uniform particle distributions in both mid-plane and cross-sectional contours are observed prior to the

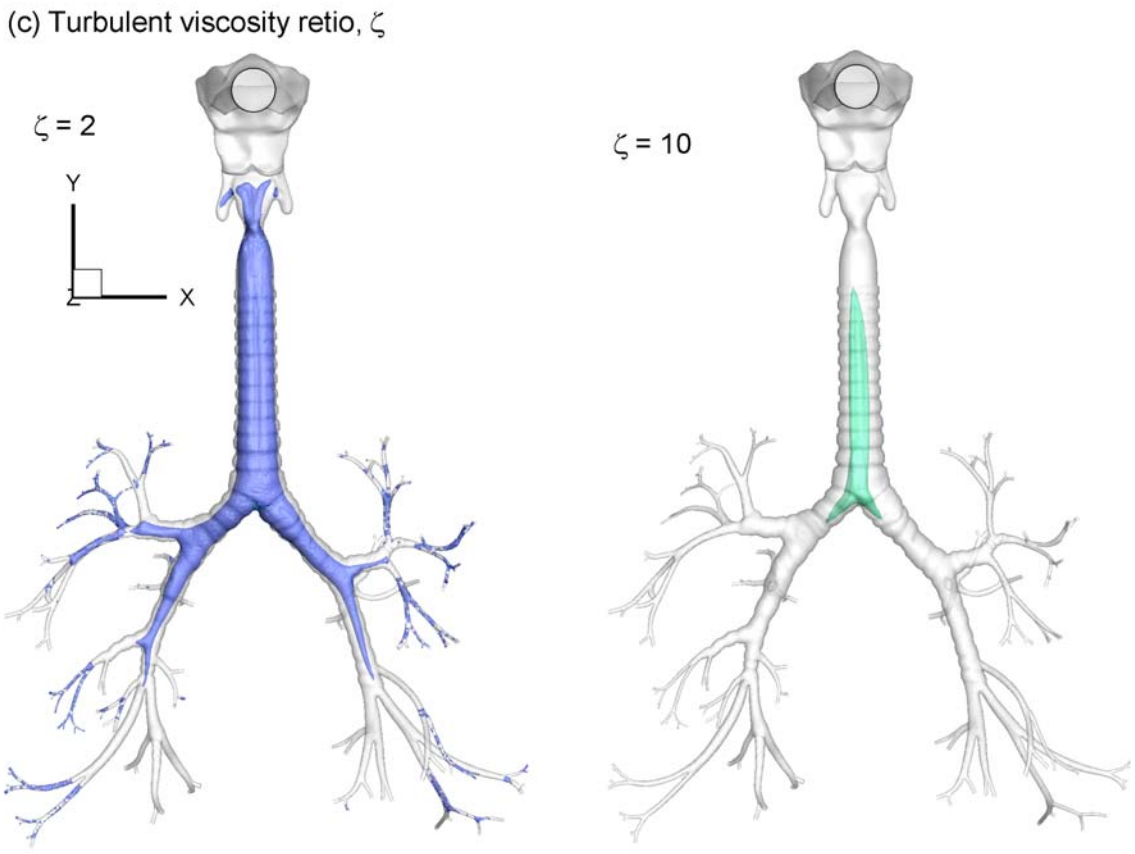

(**a**) (**b**)

Figure 4: Turbulent viscosity ratio (i.e., $\zeta = (\nu + \nu_T)/\nu$) in MT-TB geometry at an inhalation flow rate of 20 L/min:(**a**) $\zeta = 2$, and (**b**) $\zeta = 11$.

onset of turbulence. With increasingly turbulent flow, which may begin in the region of Slice 2, the concentration attenuation becomes apparent. Especially, a ring-shaped profile of vapor forms at Slice 2. The vapor concentration continues to decrease, as evident in the lower mass fraction in Slice 3. Considering that the absorption rate is proportional to the local concentration gradient, higher absorption in the M-T geometry and lower absorption in trachea are expected.

3.4. Pulmonary Uptake and Upper Airway Absorption

In this study, the pulmonary delivery efficiency or uptake is defined as the fraction of vapor exiting *via* the trachea outlet to the vapor that is administrated. Anesthetic vapor inhaled into the airway must escape the filtration of the conducting airway before entering the pulmonary region where capillary vessels are rich. In contrast, the conducting airway, which extends from the mouth to G15, is mainly lined with smooth muscles. Figure **6** shows the comparison of pulmonary uptake between two anesthetic vapors, i.e., xenon and isoflurane in the five lobes. The diffusivities of these two vapors are at the same magnitude (~0.08 cm^2/s). However, their solubility in water differs significantly. Xenon is highly soluble in water and has an air-wall ratio λ_{a-w} of 460, while isoflurane is only slightly soluble in water and has a much smaller air-wall ratio (λ_{a-w} = 0.62) [65]. Due to larger wall absorption loss to the conducting airway, xenon has a much lower pulmonary dosage (~52%) compared to isoflurane (~96%) under quiet breathing conditions (20 L/min). The lobar dosages for both species are generally consistent with the flow partitions into each lobe (Figure **6**).

Figure **7** shows the wall absorption for species with high and low solubility that corresponds to xenon and isoflurane, respectively. For generality, a wide range of diffusivities were considered for three inhalation flow rates (10, 20, 30 L/min). Again, species with a higher water solubility are absorbed into wall at a much high rate for all breathing scenarios considered. In this study, the wall absorption with λ_{a-w} = 460 is more than 8 times larger than that with λ_{a-w} = 0.62. For a given vapor, the wall absorption decrease as the inhalation rate increase, due to the shorter residence time in the conducting airways.

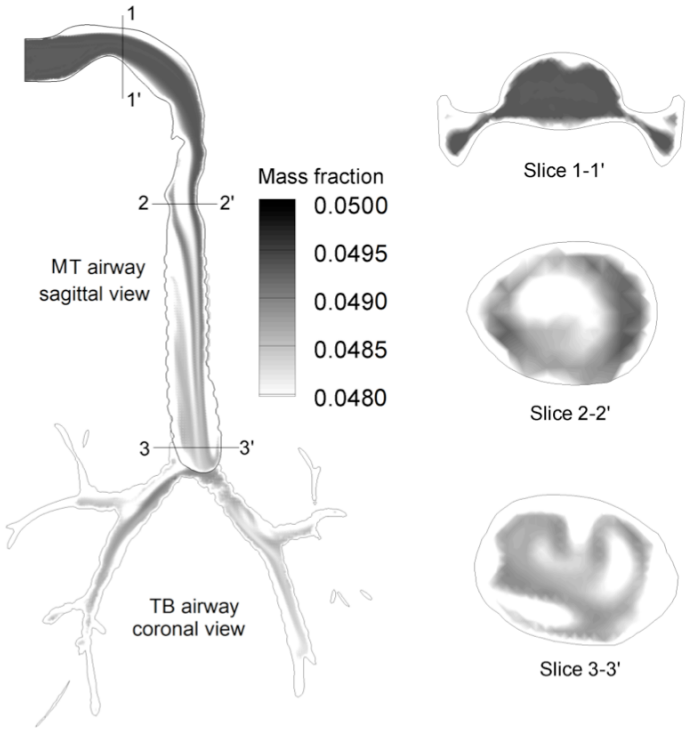

Figure 5: Midplane and cross-sectional concentration profiles of xenon in the MT-TB airway. Slice 2 represents the glottis.

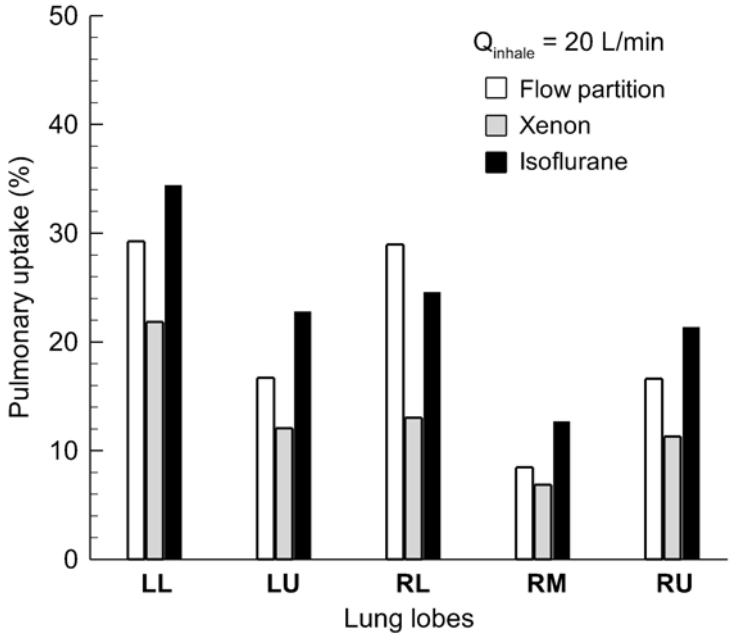

Figure 6: Comparison of Pulmonary uptake between xenon and isoflurane under quiet breathing conditions. The inhaled airflow partition into the five lobes was also plotted. LL: left lower; LU: left upper; RL: right lower; RM: right middle; RU: right upper.

3.5. Local Absorption Results

Local absorption patterns in the upper airway are displayed in Figure **8** for the two anesthetic species of xenon and isoflurane. The deposition enhancement factor (DEF) that was generally used for particle depositions [66-69] will be borrowed in this study to signify the ratio of local to averaged absorption rate of inhaled agents. In this study, the local area was assumed to be a region with a diameter of 500 μm, or approximately 50 lung epithelial cells in length [70].

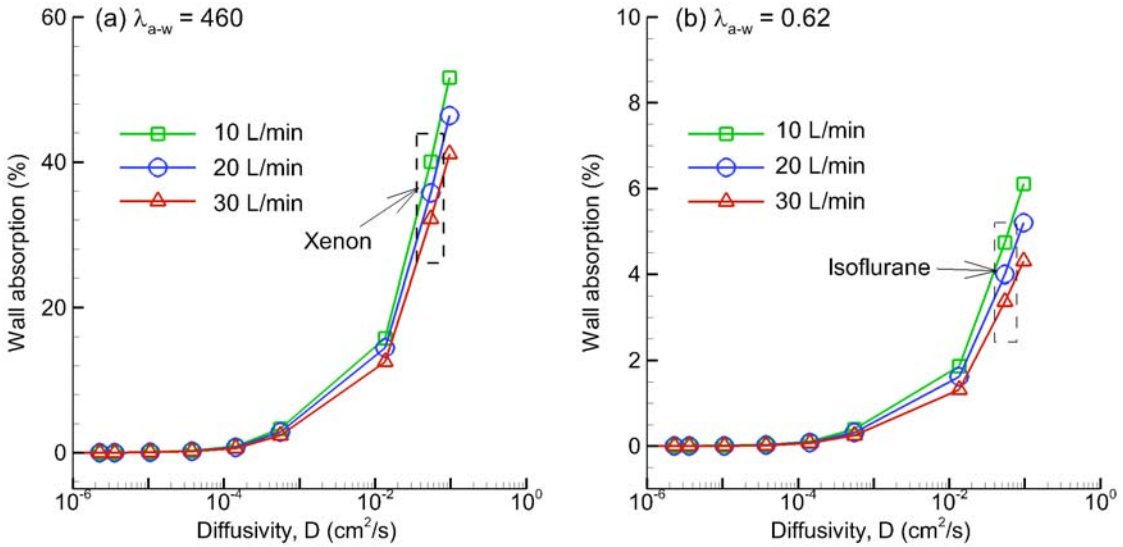

Figure 7: Wall absorption as a function of diffusivity for vapor species with (**a**) high solubility in water (λ_{a-w} = 460), and (**b**) low solubility in water (λ_{a-w} = 0.62).

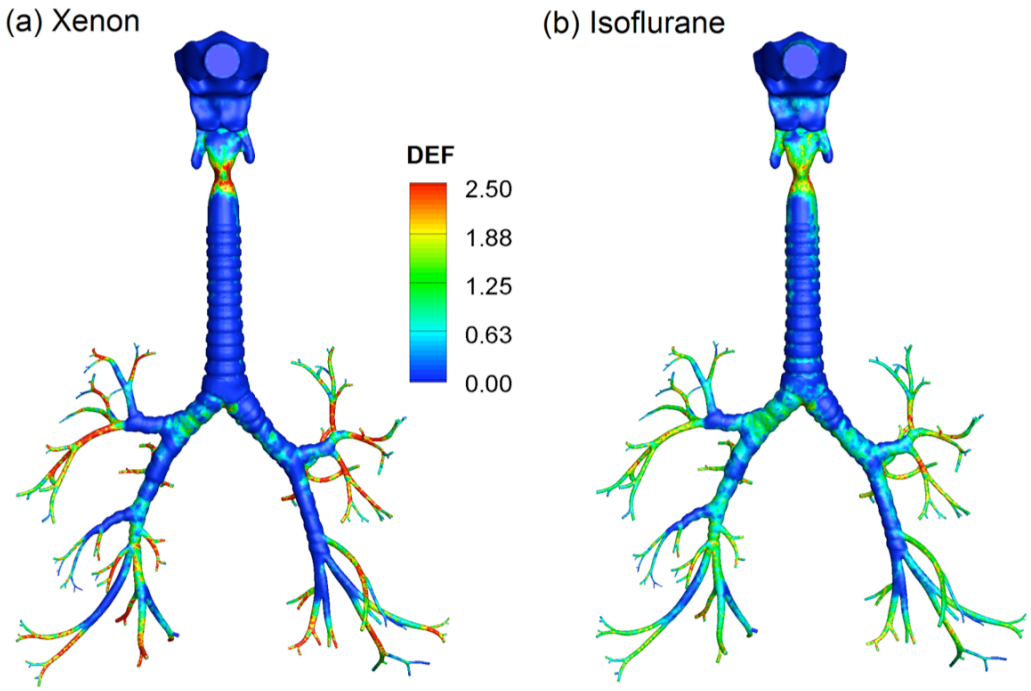

Figure 8: Local absorption pattern of nanoparticles in the MT-TB model in terms of deposition enhancement factor (DEF) for (**a**) xenon, and (**b**) isoflurane.

The overall pattern of DEF appears very similar between xenon and isoflurane. Both cases display absorption hot spots around the glottis where convective diffusion is high due to converging-diverging flows. Elevated DEF values are also observed in the bifurcations from G5 to G9 for both particle sizes, with more elevated DEFs in the more distal bronchioles and presumably due to deceasing bronchiolar diameters. This finding is noteworthy, because the absorption loss of inhaled anesthetics in the airway could be much larger than predicted in this study because of the even smaller bronchiolar diameters of further generations. Furthermore, for any two successive generations, the number of bronchioles increases by twice and the total surface areas of a more distal generation increase too. The primary difference between these two species is the intensity of the DEF hot spots. These hot spots are more pronounced for xenon vapor in the glottis and

distal bronchioles. In contrast, a more dispersed DEF distribution is observed for isoflurane. There are absorptions of isoflurane in the pharynx and tracheal cartilaginous rings, while this absorptions is absent for xenon.

3.6. Cross-Sectional Particle Profiles

Cross-sectional particle profiles exiting the TB geometry have a significant impact on downstream absorptions throughout the lung. One open question is: can we assume evenly distributed aerosol profiles after G9? Or, how accurate of such an assumption? Answer to this question will have important implications on interpolating the results from existing whole lung models. In this study, we examined existing profiles of xenon at three G9 bronchiolar outlets, as shown in Figure **9**. First, these three exiting profiles appear visually similar, with each exhibiting a skewed peak concentration. Second, the vapor concentrations at all outlets have been significantly diluted, which is about 20% − 40% of the inhaled concentrations. It is interesting to note that the vapor concentration at the outlets could vary dramatically, as evident in the mass fraction of 0.02 at the outlets "*a*" and "*b*" in contrast to 0.01 at the outlet "*c*".

4. CONCLUSION

Vapor transport and absorption in an upper airway model extending to G9 has been simulated with anesthetic vapor species. Highly heterogeneous airflow patterns were observed even in the most peripheral bronchioles (G9) considered in this study. Similarly, large variations of bronchiolar vapor concentrations were observed among the five lobes. The concentration level of anesthetic vapor in the pulmonary bronchioles could be much lower than administered concentrations. Vapor depletion due to wall absorption can be significant (~50%) for highly soluble anesthetics and is insignificant for low solubility ones. The predicted pulmonary delivery efficiency is ~52% for xenon and ~96% for isoflurane under quiet breathing conditions. Factors influencing the onset and duration of anesthesia include inspired concentration, ventilation, anesthetic solubility, cardiac output, and

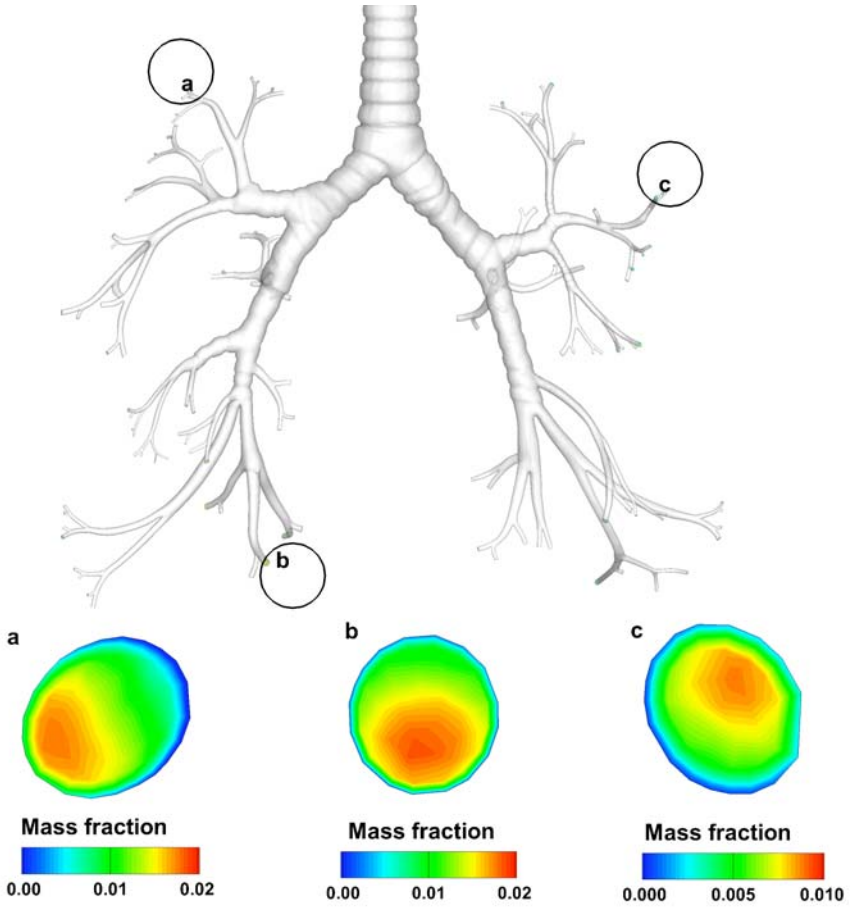

Figure 9: Outlet concentration profiles for xenon at the G9 bronchioles in (**a**) right upper lobe, (**b**) right lower lobe, and (**c**) left upper lobe.

tissue capacity. A higher inspired concentration and better alveolar ventilation will result in a higher alveolar anesthetic concentration, which in turn induce a quicker onset. The uptake of inhaled anesthetics by the blood (wash-in) is mainly determined by the solubility. A vapor with a lower solubility (such as isoflurane) will reach the alveolar-blood equilibration faster and will have a quicker induction and recovery.

Limitations of the current study include the assumptions of steady state flows, neglecting reactions, a composite mucus-tissue layer, and a rigid airway surface. Tidal breathing could notably affect the inspiration flow pattern and affect the motion of entrained vapors. The movement of the airway surface during a breathing cycle could also exert a noticeable effect on respiratory flows and vapor dynamics. Steady inhalations were adopted in this study to avoid the prohibitive computational expense required for tidal breathings. Based on a mesh size of 6 million, one steady simulation in this study took about 20 hours in an Intel 2.27 GHz workstation. By contrast, one transient breathing cycle with 50 time steps would take about 1,000 hours. Further numerical analyses and complimentary *in vivo* studies are needed to better evaluate the effects of tidal flows, compliable walls, and intra-subject variability to improve predictions of the anesthetic dosage and potency.

ACKNOWLEDGEMENTS

This work was sponsored in part by Central Michigan University (CMU) Innovational Research Grant P421071 and Early Career Grant P622911. Jordan Rohlinger is gratefully acknowledged for helpful discussions and for reviewing the manuscript.

REFERENCES

[1] Kvolik S, Glavas-Obrovac L, Bares V, Karner I. Effects of inhalation anesthetics halothane, sevoflurane, and isoflurane on human cell lines. Life Sci 2005; 77(19): 2369-83. http://dx.doi.org/10.1016/j.lfs.2004.12.052

[2] Haghighi SS, Madsen R, Green KD, Oro JJ, Kracke GR. Suppression of motor evoked potentials by inhalation anesthetics. J Neurosurg Anesthesiol 1990; 2(2): 73-78. http://dx.doi.org/10.1097/00008506-199006000-00003

[3] Campagna JA, Miller KW, Forman SA, Mechanisms of Actions of Inhaled Anesthetics. New Engl J Med 2003; 348(21): 2110-24. http://dx.doi.org/10.1056/NEJMra021261

[4] Maciver MB, Roth SH. Inhalation anaesthetics exhibit pathway-specific and differential actions on hippocampal synaptic responses *in vitro*. Br J Anaesthesia 1988; 60(6): 680-91. http://dx.doi.org/10.1093/bja/60.6.680

[5] Merkel G, Eger EI. A comparative study of halothane and halopropane anesthesia including method for determining equipotency. Anesthesiology 1963; 24(3): 346-&. http://dx.doi.org/10.1097/00000542-196305000-00016

[6] Fiserova-Bergerova V, Holaday DA. Uptake and Clearance of Inhalation Anesthetics in Man. Drug Metab Rev 1979; 9(1): 43-60. http://dx.doi.org/10.3109/03602537909046433

[7] Cheng KH, Cheng YS, Yeh HC, Guilmette RA, Simpson SQ, Yang SQ, Swift DL. *In vivo* measurements of nasal airway dimensions and ultrafine aerosol depositing in human nasal and oral airways. J Aerosol Sci 1996; 27: 785-801. http://dx.doi.org/10.1016/0021-8502(96)00029-8

[8] Kim JW, Xi J, Si XA. Dynamic growth and deposition of hygroscopic aerosols in the nasal airway of a 5-year-old child. Int J Numer Methods Biomed Eng 2013; 29(1): 17-39. http://dx.doi.org/10.1002/cnm.2490

[9] Si XA, Xi J, Kim J, Zhou Y, Zhong H. Modeling of release position and ventilation effects on olfactory aerosol drug delivery. Respir Physiol Neurobiol 2013; 186(1): 22-32. http://dx.doi.org/10.1016/j.resp.2012.12.005

[10] Xi J, Berlinski A, Zhou Y, Greenberg B, Ou X. Breathing Resistance and Ultrafine Particle Deposition in Nasal-Laryngeal Airways of a Newborn, an Infant, a Child, and an Adult. Annals Biomed Eng 2012; 40(12): 2579-95. http://dx.doi.org/10.1007/s10439-012-0603-7

[11] Zhao K, Scherer PW, Hajiloo SA, Dalton P. Effect of anatomy on human nasal air flow and odorant transport patterns: Implications for olfaction. Chem Senses 2004; 29(5): 365-79. http://dx.doi.org/10.1093/chemse/bjh033

[12] Heyder J, Gebhart J, Rudolf G, Schiller CF, Stahlhofen W. Deposition of particles in the human respiratory tract in the size range of 0.005 - 15 microns. J Aerosol Sci 1986; 17(5): 811-25. http://dx.doi.org/10.1016/0021-8502(86)90035-2

[13] Jaques PA, Kim CS. Measurement of total lung deposition of inhaled ultrafine particles in healthy men and women. Inhalation Toxicol 2000; 12(8): 715-31. http://dx.doi.org/10.1080/08958370050085156

[14] Kim CS, Jaques PA. Analysis of total respiratory deposition of inhaled ultrafine particles in adult subjects at various breathing patterns. Aerosol Sci Technol 2004; 38(6): 525-40. http://dx.doi.org/10.1080/02786820490465513

[15] Morawska L, Hofmann W, Hitchins-Loveday J, Swanson C, Mengersen K. Experimental study of the deposition of combustion aerosols in the human respiratory tract. J Aerosol Sci 2005; 36: 939-57. http://dx.doi.org/10.1016/j.jaerosci.2005.03.015

[16] Stahlhofen W, Rudolf G, James AC. Intercomparison of experimental regional aerosol deposition data. J Aerosol Med 1989; 2(3): 285-308. http://dx.doi.org/10.1089/jam.1989.2.285

[17] Heenan AF, Matida E, Pollard A, Finlay WH. Experimental measurements and computational modeling of the flow field in an idealized human oropharynx. Exper Fluids 2003; 35(1): 70-84. http://dx.doi.org/10.1007/s00348-003-0636-7

[18] Johnstone A, Uddin M, Pollard A, Heenan A, Finlay WH. The flow inside an idealised form of the human extra-thoracic airway. Exper Fluids 2004; 37: 673-89. http://dx.doi.org/10.1007/s00348-004-0857-4

[19] Zhang Y, Chia TL, Finlay WH. Experimental measurement and numerical study of particle deposition in highly idealized mouth-throat models. Aerosol Sci Technol 2006; 40(5): 361-72. http://dx.doi.org/10.1080/02786820600615055

[20] Zhang Y, Finlay WH, Matida EA. Particle deposition measurements and numerical simulation in a highly idealized mouth-throat. J Aerosol Sci 2004; 35(7): 789-803. http://dx.doi.org/10.1016/j.jaerosci.2003.12.006

[21] Cheng KH, Cheng YS, Yeh HC, Swift DL. An experimental method for measuring aerosol deposition efficiency in the human oral airway. Am Ind Hyg Assoc J 1997; 58: 207-13. http://dx.doi.org/10.1080/15428119791012856

[22] Cheng YS, Su YF, Yeh HC, Swift DL. Deposition of Thoron progeny in human head airways. Aerosol Sci Technol 1993; 18: 359-75. http://dx.doi.org/10.1080/02786829308959610

[23] Frederick CB, Bush ML, Lomax LG, Black KA, Finch L, Kimbell JS, *et al*. Application of a hybrid computational fluid dynamics and physiologically based inhalation model for interspecies dosimetry extrapolation of acidic vapors in the upper airways. Toxicol Appl Pharmacol 1998; 152(1): 211-31. http://dx.doi.org/10.1006/taap.1998.8492

[24] Kimbell JS, Subramaniam RP. Use of computational fluid dynamics models for dosimetry of inhaled gases in the nasal passages. Inhalation Toxicol 2001; 13(5): 325-34. http://dx.doi.org/10.1080/08958370151126185

[25] Shi H, Kleinstreuer C, Zhang Z. Laminar airflow and nanoparticle or vapor deposition in a human nasal cavity model. J Biomech Eng-Trans Asme 2006; 128(5): 697-706. http://dx.doi.org/10.1115/1.2244574

[26] Zhang Z, Kleinstreuer C. Species heat and mass transfer in a human upper airway model. Int J Heat Mass Transfer 2003; 46(25): 4755-68. http://dx.doi.org/10.1016/S0017-9310(03)00358-2

[27] Hofmann W, Golser R, Balashazy I. Inspiratory deposition efficiency of ultrafine particles in a human airway bifurcation model. Aerosol Sci Technol 2003; 37(12): 988-94. http://dx.doi.org/10.1080/02786820300898

[28] Xi J, Longest PW, Martonen TB. Effects of the laryngeal jet on nano- and microparticle transport and deposition in an approximate model of the upper tracheobronchial airways. J Appl Physiol 2008; 104(6): 1761-77. http://dx.doi.org/10.1152/japplphysiol.01233.2007

[29] Taylor AB, Borhan A, Ultman JS. Three-dimensional simulations of reactive gas uptake in single airway bifurcations. Annals Biomed Eng 2007; 35(2): 235-49. http://dx.doi.org/10.1007/s10439-006-9195-4

[30] Zhao K, Scherer PW, Hajiloo SA, Dalton P. Effects of anatomy on human nasal air flow and odorant transport patterns: Implictions for olfaction. Chem Senses 2004; 29(5): 365-79. http://dx.doi.org/10.1093/chemse/bjh033

[31] Keyhani K, Schere, PW, Mozell MM. A numerical model of nasal odorant transport for the analysis of human olfaction. J Theoretical Biol 1997; 186(3): 279-301. http://dx.doi.org/10.1006/jtbi.1996.0347

[32] Tian G, Longest PW. Application of a new dosimetry program TAOCS to assess transient vapour absorption in the upper airways. Inhalation Toxicol 2010; 22(13): 1047-63. http://dx.doi.org/10.3109/08958378.2010.521783

[33] Tian G, Longest PW. Development of a CFD Boundary Condition to Model Transient Vapor Absorption in the Respiratory Airways. J Biomech Eng-Trans Asme 2010; 132(5).

[34] Tian G, Longest PW, Su G, Hindle M. Characterization of Respiratory Drug Delivery with Enhanced Condensational Growth using an Individual Path Model of the Entire Tracheobronchial Airways. Annals Biomed Eng 2011; 39(3): 1136-53. http://dx.doi.org/10.1007/s10439-010-0223-z

[35] Xi J, Longest PW. Transport and deposition of micro-aerosols in realistic and simplified models of the oral airway. Annals Biomed Eng 2007; 35(4): 560-81. http://dx.doi.org/10.1007/s10439-006-9245-y

[36] Cheng KH, Cheng YS, Yeh HC, Swift DL. Measurements of airway dimensions and calculation of mass transfer characteristics of the human oral passage. J Biomech Eng 1997; 119: 476-82. http://dx.doi.org/10.1115/1.2798296

[37] Yeh HC, Schum GM. Models of human lung airways and their application to inhaled particle deposition. Bull Math Biol 1980;42: 461-80.

[38] ICRP. Human Respiratory Tract Model for Radiological Protection, Elsevier Science Ltd, New York 1994.

[39] Cohen BS, Sussman RG, Lippmann M. Ultrafine particle deposition in a human tracheobronchial cast. Aerosol Sci Technol 1990; 12: 1082-93. http://dx.doi.org/10.1080/02786829008959418

[40] Russo J, Robinson R, Oldham MJ. Effects of cartilage rings on airflow and particle deposition in the trachea and main bronchi. Med Eng Phys 2008; 30: 581-89. http://dx.doi.org/10.1016/j.medengphy.2007.06.010

[41] Horsfield K, Dart G, Olson DE, Cumming G. Models of the human bronchial tree. J Appl Physiol 1971; 31: 207-17.

[42] Hammersley JR, Olson DE. Physical models of the smaller pulmonary airways. J Appl Physiol 1992; 72: 2402-14.

[43] Heistracher T, Hofmann W. Physiologically realistic models of bronchial airway bifurcations. J Aerosol Sci 1995; 26(3): 497-509. http://dx.doi.org/10.1016/0021-8502(94)00113-D

[44] Ghalichi F, Deng X, Champlain AD, Douville Y, King M, Guidoin R. Low Reynolds number turbulence modeling of blood flow in arterial stenoses. Biorheology 1998; 35(4&5): 281-94. http://dx.doi.org/10.1016/S0006-355X(99)80011-0

[45] Wilcox DC. Turbulence Modeling for CFD, 2nd ed, DCW Industries, Inc, California 1998.

[46] Zhang Z, Kleinstreuer C. Low-Reynolds-number turbulent flows in locally constricted conduits: A comparison study. AIAA J 2003; 41(5): 831-40. http://dx.doi.org/10.2514/2.2044

[47] Zhang Z, Kleinstreuer C. Airflow structures and nano-particle deposition in a human upper airway model. J Comput Phys 2004; 198(1): 178-10. http://dx.doi.org/10.1016/j.jcp.2003.11.034

[48] Longest PW, Vinchurkar S. Validating CFD predictions of respiratory aerosol deposition: effects of upstream transition and turbulence. J Biomech 2006; (in press).

[49] Allen MD, Raabe OG. Slip correction measurements of spherical solid aerosol particles in an improved Millikan apparatus. Aerosol Sci Technol 1985; 4: 269-86. http://dx.doi.org/10.1080/02786828508959055

[50] Cheng YS, Zhou Y, Chen BT. Particle deposition in a cast of human oral airways. Aerosol Sci Technol 1999; 31: 286-300. http://dx.doi.org/10.1080/027868299304165

[51] Balashazy I, Hofmann W. Particle deposition in airway bifurcations-I. Inspiratory flow. J Aerosol Sci 1993; 24: 745-72. http://dx.doi.org/10.1016/0021-8502(93)90044-A

[52] Martonen TB, Guan X, Schreck RM. Fluid dynamics in airway bifurcations: I. Primary flows. Inhalation Toxicol 2001; 13(4): 261-79. http://dx.doi.org/10.1080/089583701750127359

[53] Zhang Z, Kleinstreuer C. Effect of particle inlet distributions on deposition in a triple bifurcation lung airway model. J Aerosol Med-Deposit Clearance Effects Lung 2001; 14(1): 13-29. http://dx.doi.org/10.1089/08942680152007864

[54] Zhang Z, Kleinstreuer C, Kim CS. Flow structure and particle transport in a triple bifurcation airway model. J Fluids Eng-Trans ASME 2001; 123(2): 320-30. http://dx.doi.org/10.1115/1.1359525

[55] Tovbin YK, Rahinovich AB. Self-diffusion, mass transfer, and viscosity coefficients for a binary mixture in narrow slit-like pores. Russian Chem Bull 2005; 54(8): 1777-86. http://dx.doi.org/10.1007/s11172-006-0036-2

[56] Pritchard DT, Currie JA. Diffusion of coefficients of carbon dioxide, nitrous oxide, ethylene and ethane in air and their measurement. J Soil Sci 1982; 33(2): 175-84. http://dx.doi.org/10.1111/j.1365-2389.1982.tb01757.x

[57] Longest PW, Xi J. Effectiveness of direct Lagrangian tracking models for simulating nanoparticle deposition in the upper airways. Aerosol Sci Technol 2007; 41: 380-97. http://dx.doi.org/10.1080/02786820701203223

[58] Matida EA, Finlay WH, Grgic LB. Improved numerical simulation of aerosol deposition in an idealized mouth-throat. J Aerosol Sci 2004; 35: 1-19. http://dx.doi.org/10.1016/S0021-8502(03)00381-1

[59] Xi J, Longest PW. Effects of improved near-wall modeling on micro-particle deposition in oral airway geometries. Proceedings of the 2007 ASME Summer Bioengineering Conference, Keystone, CO. 2007; Paper No. SBC2007-176227.

[60] Corcoran TE, Chigier N. Inertial deposition effects: A study of aerosol mechanics in the trachea using laser doppler velocity and fluorescent dye. J Biomech Eng 2002; 124: 629-37. http://dx.doi.org/10.1115/1.1516572

[61] Pelorson X, Hirschberg A, van Hassel RR, Wijnands APJ, Auregan Y. Theoretical and experimental study of quasisteady-flow separation within the glottis during phonation. Application to a modified two-mass model. J Acoust Soc Am 1994; 96: 3416-31. http://dx.doi.org/10.1121/1.411449

[62] Scherer RC, Titze IR, Curtis JF. Intraglottal pressure profiles for a symmetric and oblique glottis with a divergence angle of 10 degrees. J Acoust Soc Am 2001; 109: 1616-30. http://dx.doi.org/10.1121/1.1333420

[63] Asgharian B, Anjilvel S. A Monte Carlo calculation of the deposition efficiency of inhaled particles in lower airways. J Aerosol Sci 1994; 25(4): 711-21. http://dx.doi.org/10.1016/0021-8502(94)90012-4

[64] Zhang Z, Kleinstreuer C, Kim CS. Airflow and Nanoparticle Deposition in a 16-Generation Tracheobronchial Airway Model. Annals Biomed Eng 2008; 36(12): 2095-10. http://dx.doi.org/10.1007/s10439-008-9583-z

[65] WebBook, N.C, 2008; http://webbook.nist.gov/chemistry/."

[66] Kim J, Xi J, Si X, Berlinski A, Su WC. Hood Nebulization: Effects of Head Direction and Breathing Mode on Particle Inhalability and Deposition in a 7-Month-Old Infant Model. Journal of aerosol medicine and pulmonary drug delivery, 2013; in press.

[67] Xi J, Kim J, Si XA, Zhou Y. Diagnosing Obstructive Respiratory Diseases using Exhaled Aerosol Fingerprints: A Feasibility Study. J Aerosol Sci 2013. http://dx.doi.org/10.1016/j.jaerosci.2013.06.003

[68] Xi J, Kim J, Si XA, Zhou Y. Hygroscopic aerosol deposition in the human upper respiratory tract under various thermo-humidity conditions. J Environ Sci Health Part A 2013; 48(14): 1790-805. http://dx.doi.org/10.1080/10934529.2013.823333

[69] Xi J, Si X, Zhou Y, Kim J, Berlinski A. Growth of Nasal-Laryngeal Airways in Children and Their Implications in Breathing and Inhaled Aerosol Dynamics. Respiratory Care 2013; in press.

[70] Lumb AB. Nunn's Applied Respiratory Physiology, Butterworth Heinemann, Oxford 2000.

Received on 28-09-2013 Accepted on 08-10-2013 Published on 27-11-2013

DOI: http://dx.doi.org/10.14205/2310-9394.2013.01.01.2